

Stratospheric Age-of-Air: Sensitivity to Finite Volume Remapping Algorithm

Clara Orbe ^{1,2}, Lawrence L. Takacs ³, Amal El Akkraoui ³,
Krzysztof Wargan ³, Andrea Molod ³

¹NASA Goddard Institute for Space Studies, New York, NY

²Department of Applied Physics and Applied Mathematics, Columbia University, New York, NY

³Global Modeling and Assimilation Office, NASA Goddard Space Flight Center, Greenbelt, MD

Key Points:

- The stratospheric mean age-of-air simulated in GEOS-5 is sensitive to the remapping scheme used within the finite-volume dynamical core.
- This sensitivity in the age-of-air approaches 30% and imprints on the simulated distributions of several long-lived chemical trace gases, including nitrous oxide and methane.
- The age-of-air sensitivities primarily reflect changes in resolved wave convergence over the Northern Hemisphere midlatitude stratosphere, which impact mean upwelling within the tropical lower stratosphere.

Corresponding author: =name=, =email address=

17 **Abstract**

18 Accurately modeling the large-scale transport of trace gases and aerosols is critical
 19 for interpreting past (and projecting future) changes in atmospheric composition.
 20 Simulations of the stratospheric mean age-of-air continue to show persistent biases among
 21 chemistry climate models, although the drivers of these biases are not well understood.
 22 Here we identify one driver of simulated stratospheric transport differences among various
 23 NASA Goddard Earth Observing System Version 5 (GEOS-5) candidate model ver-
 24 sions under consideration for the upcoming GEOS-5 Retrospective analysis for the 21st
 25 Century (GEOS-R21C). In particular, we show that the simulated age-of-air values are
 26 sensitive to the so-called “remapping” algorithm used within the finite-volume dynam-
 27 ical core, which controls how individual material surfaces are vertically interpolated back
 28 to standard pressure levels after each horizontal advection time step. Differences in the
 29 age-of-air resulting from changes within the remapping algorithm approach ~ 1 year over
 30 the high latitude middle stratosphere - or about 30% climatological mean values - and
 31 imprint on several trace gases, including methane (CH_4) and nitrous oxide (N_2O). These
 32 transport sensitivities reflect, to first order, changes in the strength of tropical upwelling
 33 which are driven by changes in resolved wave convergence over northern midlatitudes
 34 as (critical lines of) wave propagation shift in latitude. Finally, we show that degrada-
 35 tions in the simulation of the age-of-air, stratospheric upwelling and zonal wind climate
 36 statistics derived from 30-year-long atmosphere-only (AMIP) experiments, translate to
 37 degraded skill in the analysis states used within data assimilation experiments. Our re-
 38 sults strongly support continued examination of the role of numerics in contributing to
 39 transport biases in composition modeling.

40 **Plain Language Summary**

41 Large-scale transport plays a crucial role in distributing climatically important trace
 42 constituents in the atmosphere, especially in the stratosphere where transport largely
 43 determines the chemical lifetimes of trace gases. One summary of transport in the strato-
 44 sphere is the “mean age” or the mean transit time since air at a point in the stratosphere
 45 was last in the troposphere. Current models used for simulating stratospheric compo-
 46 sition produce a range of simulated ages, although these differences are poorly under-
 47 stood. Among other factors, model numerics play a critical role in transport, but few
 48 studies have explored the sensitivity of the mean age to the choice of numerical scheme
 49 employed within different dynamical cores. Here we use one model to show that the mean
 50 age is sensitive to the so-called “remapping” algorithm used within the finite-volume dy-
 51 namical core that controls how individual material surfaces are vertically interpolated
 52 back to standard pressure levels after each horizontal advection time step. This reflects
 53 sensitivities in the representation of how waves propagate from the troposphere into the
 54 stratosphere. This work suggests that model numerics can be an important factor in con-
 55 tributing to differences in simulated transport among models.

56 **1 Introduction**

57 The chemical and radiative properties of the troposphere and lower stratosphere
 58 are strongly influenced by the stratosphere-troposphere exchange of mass and tracers (e.g.,
 59 Morgenstern and Carver (2001); Hegglin et al. (2006); Pan et al. (2007)). Properly sim-
 60 ulating the stratospheric circulation and its influence on atmospheric composition in earth
 61 system models is important for capturing past decadal trends in surface climate, par-
 62 ticularly in response to changes in Southern Hemisphere ozone depletion (e.g., Son et
 63 al. (2009); Polvani et al. (2011)). In the Northern Hemisphere (NH), the stratospheric
 64 circulation’s coupling to ozone could represent an important feedback on the climate’s
 65 response to future increases in greenhouse gases (GHGs), especially over the North At-
 66 lantic (e.g., Chiodo and Polvani (2019)). On shorter subseasonal timescales, stratospheric

67 ozone changes associated with strong polar vortex states may also modulate Arctic sea
68 level pressure and surface temperatures (e.g., Ivy et al. (2017); Oehrlein et al. (2020)),
69 so much so that seasonal forecast systems employing prognostic ozone show suggestions
70 of increased signal-to-noise ratio in predictions of the North Atlantic Oscillation (B. M. Monge-
71 Sanz et al. (2022)).

72 Key to accurately simulating a consistent representation of coupling between strato-
73 spheric dynamics and chemical trace gases is ensuring that a model’s underlying trans-
74 port circulation is properly represented. To this end, much effort has been paid to de-
75 veloping and refining so-called “tracer-independent” metrics of transport (Holzer and Hall
76 (2000)) such as the mean age-of-air (Hall and Plumb (1994)) and to applying these mea-
77 sures to rigorously evaluate model transport characteristics in chemistry climate mod-
78 els (CCMs) (e.g., Hall et al. (1999); Orbe et al. (2018); Dietmüller et al. (2018); Aba-
79 los et al. (2020)).

80 While the assessment of CCMs participating in the SPARC Chemistry Climate Model
81 Validation (SPARC CCMVal) effort showed a marked improvement in simulated trans-
82 port characteristics relative to previous intercomparisons (J. Neu et al. (2010)), more re-
83 cent analysis of models participating in the SPARC Chemistry Climate Modeling Ini-
84 tiative (CCMI) (Eyring et al. (2013)) do not demonstrate any improvement (Dietmüller
85 et al. (2018), see their Figure 3). In particular, although some models produce mean age
86 values that agree well with observational estimates, the CCMI intermodel spread is ~
87 50%, with models generally simulating transport that is too vigorous, relative to obser-
88 vations. While documenting these transport differences among models is straightforward,
89 understanding the drivers of this spread remains a key challenge and there is still no con-
90 sensus on the main drivers of simulated age biases among the current generation of CCMs.

91 A key challenge in identifying the drivers of age-of-air – and other stratospheric trans-
92 port – biases is that they reflect the time-integrated effects of advection by the residual
93 mean circulation and eddy diffusive mixing, or the quasi-random transport due to the
94 breaking of Rossby waves (e.g., Holton et al. (1995); Plumb (2002)). Given that the in-
95 fluences of mixing and advection are not easily separable, studies have come to differ-
96 ent conclusions about the drivers of age biases in models. In particular, the analysis of
97 the CCMVal models showed a strong correlation between the intermodel spread in the
98 age-of-air and lower stratospheric tropical upwelling, whereas Dietmüller et al. (2018)
99 showed that the age spread among the CCMI models was driven by differences in mix-
100 ing. While future attempts to further distinguish between these drivers of age biases us-
101 ing either simplified “leaky pipe” models (Plumb (1996); J. L. Neu and Plumb (1999))
102 or more complete measures of the transport circulation such as the “age spectrum” (e.g.,
103 Hall and Plumb (1994); Waugh and Hall (2002)) may prove enlightening, at present there
104 is no consensus on what is driving biases in the simulated age-of-air in models.

105 One potential limitation of using multi-model intercomparisons to understand drivers
106 of age biases is that many aspects of model formulation can influence both stratospheric
107 upwelling and mixing. Thus, while intercomparisons are useful for identifying common
108 model biases, understanding the drivers of these biases is difficult absent single model-
109 based process studies. Among these, several aspects of model formulation have been iden-
110 tified as influencing simulated mean age distributions. As the mean age is sensitive to
111 vertical motion in the lowermost stratosphere, these include large sensitivities to verti-
112 cal resolution (Orbe et al. (2020)) and to spurious vertical mixing either introduced in
113 vertical coordinate transformations in offline chemical transport models (B. Monge-Sanz
114 et al. (2007)) or through use of assimilated winds performed either in offline (e.g., Legras
115 et al. (2004)) or online data assimilation and “nudged” configurations (e.g., Pawson et
116 al. (2007); Orbe et al. (2017); Davis et al. (2022)). These age sensitivities can be still fur-
117 ther amplified, depending on whether or not parameterized gravity waves are included
118 (Eichinger et al. (2020)).

119 By comparison, sensitivities of the mean age to underlying tracer numerics have
 120 been less well examined, although Eluszkiewicz et al. (2000) documented a large sensi-
 121 tivity in simulated age-of-air values to the choice of advection scheme. More recently,
 122 Gupta et al. (2020) showed differences of $\sim 25\%$ in the age-of-air across identical exper-
 123 iments performed using four different dynamical cores, especially between those using
 124 spectral versus finite-volume schemes. The experiments employed in that study, how-
 125 ever, were highly idealized and it is not clear if the strong influence of tracer numerics
 126 that they identified is also realized in more comprehensive model simulations with moist
 127 physics, especially in the context of model development as carried out in operational mod-
 128 eling centers.

129 To this end, here we document the sensitivity of the stratospheric mean age in sev-
 130 eral recent versions of the NASA Goddard Earth Observing System Version 5 (GEOS-
 131 5) general circulation model (Molod et al., 2015) that represent different stages in model
 132 development since MERRA-2 (Gelaro et al. (2017)). Our focus on transport evaluation
 133 is in wake of the upcoming release of the GEOS-5 Retrospective analysis for the 21st Cen-
 134 tury (GEOS-R21C), which will serve as an intermediate reanalysis between MERRA-
 135 2 and MERRA-3 (~ 2025). As GEOS-R21C will be used to drive an off-line chemistry
 136 reanalysis (GEOS-R21C-Chem) it is imperative that it produces a credible representa-
 137 tion of transport processes.

138 In particular, here we document how in the process of evaluating candidate sys-
 139 tems for GEOS-R21C we found that the mean age was ~ 1 younger than the values sim-
 140 ulated in the model version used to produce MERRA-2 (Figure 1). The model versions
 141 shown in Figure 1 reflect more than 10 years’ worth of accumulated changes in model
 142 development, most notably changes in radiation, parameterized convection and, as we
 143 focus on here, changes in the algorithm used to transform advected fields from Lagrangian
 144 levels to fixed pressure levels after each horizontal advection time step. We show that
 145 slight modifications in this so-called “remapping” algorithm are the primary driver of
 146 the age-of-air changes exhibited in recent GEOS-R21C candidate model versions, a re-
 147 sult which may have broader implications for other general circulation models using fi-
 148 nite volume (FV) dynamical cores. We begin by discussing methods in Section 2 and present
 149 key results and conclusions in Sections 3 and 4, respectively.

150 2 Methods

151 2.1 Model Configurations

152 Here we present results from several versions of GEOS-5 spanning MERRA-2 to
 153 more recent candidates for GEOS-R21C. Among these model versions, a subset are more
 154 “official” as they have been documented and/or employed in recent model intercompar-
 155 isons and are highlighted in Figure 1. In particular, these include an intermediary model
 156 version that was used in Phase 1 of CCMI and documented in Orbe et al. (2017) (Fig.
 157 1, red line). A more recent model version that was used in the CCMI Phase 2 simula-
 158 tions (correspondence with Michael Manyin) is also shown (Fig. 1, green line). These
 159 two configurations correspond to the Heracles 5.3 and Icarus 3.2 versions of the GEOS
 160 system, respectively (**Amal: I need the actual tag names**).

161 We begin by comparing 10-year (2000-2010) climatological mean zonally averaged
 162 age-of-air profiles at 50 hPa across this subset of model versions, derived from 30-year
 163 long atmosphere-only (AMIP) integrations constrained with observed sea surface tem-
 164 peratures (Figure 1). First, we note that the profiles for the CCMI Phase 1 version of
 165 the model are very close to observations (black stars), consistent with the
 166 “GEOSCCM” documented age characteristics reported in Dietmüller et al. (2018) (see
 167 their Figure 3). In addition, while passive tracers were not integrated within MERRA-
 168 2, results using the GEOS chemistry transport model (GEOS-CTM, Kouatchou et al.

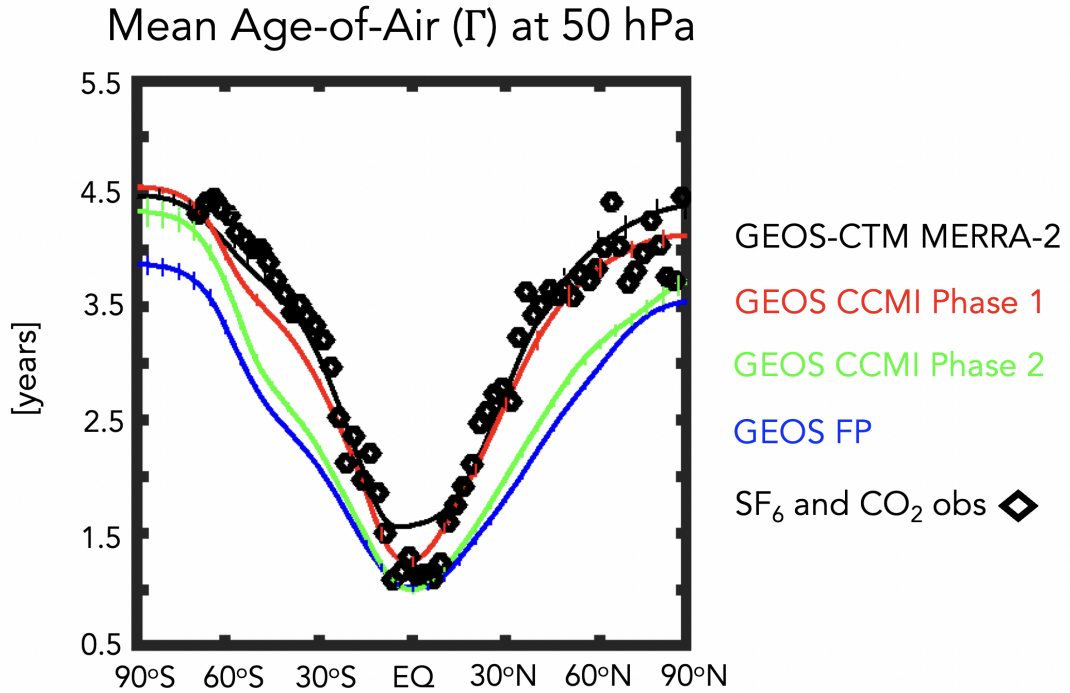


Figure 1. The 2000-2010 climatological annual mean meridional profile of the stratospheric mean age-of-air (Γ), evaluated at 50 hPa. Results from a GEOS-CTM integration constrained with MERRA-2 meteorological fields (black line) as well as free-running GEOS simulations using a model configuration for CCMI Phase 1 (red line), CCMI Phase 2 (green line) and a more recent GEOS-FP development tag (Jason 4.0, blue line) are shown. The GEOS model versions to which these configurations correspond are the Heracles 5.3, Icarus 3.2, and Jason 4.0 tags, respectively. All simulations are constrained with the same (observed) historical sea surface temperatures. Diamonds correspond to SF₆ and CO₂ in situ based estimates of Γ from Boering et al. (1996) and Engel et al. (2009). Vertical dashed lines denote $\pm\sigma$, the standard deviation of Γ over 2000-2010, for each model simulation.

169 (2015)) constrained with MERRA-2 meteorological fields (black line) also exhibits good
 170 agreement with observed values. This good agreement between the CTM-generated age-
 171 of-air and the observations is consistent with results from a previous GEOS-CTM sim-
 172 ulation (constrained with MERRA) that was documented in Orbe et al. (2017).

173 Moving to more recent development versions of the model (green and blue lines),
 174 however, reveals a reduction in the mean age by ~ 1 year over both southern and north-
 175 ern high extratropical latitudes, or a decrease of $\sim 20\text{-}30\%$ relative to MERRA-2. As dis-
 176 cussed earlier, the green line refers to the CCM Phase 2 model version, whereas the blue
 177 line refers to an undocumented candidate version (model tag Jason 4.0) that corresponds
 178 best to a model configuration similar to what is used in the GEOS forward processing
 179 (FP) numerical weather prediction system (**Amal: What is FP DAS version correspond-**
 180 **ing to Jason 4.0 (or similar model)?**). Note that this decrease in the age in both model
 181 versions is statistically significant, relative to internal variability (vertical bars on solid
 182 lines).

183 There are numerous development updates in the model that have occurred since
 184 MERRA-2. Therefore, after discussing the model configurations highlighted in Figure
 185 1 in Section 3.1, we then present results from targeted experiments aimed at successively
 186 undoing these model updates (Section 3.2). Among those aspects most likely impact-
 187 ing the stratospheric transport circulation, these include updates to the radiation scheme,
 188 moving from Chou and Suarez (1994) in the shortwave and Chou (1990, 1992) in the long-
 189 wave to the Rapid Radiative Transfer Model for GCMS (RRTGM; Iacono et al. (2008).

190 In addition to the radiation changes, another more consequential model develop-
 191 ment was made to the handling of the remapping algorithm within the model’s FV dy-
 192 namical core (Lin, 2004). In particular, vertical motion is realized through the Lagrangian
 193 transport of the “floating” vertical coordinate such that after each horizontal advection
 194 step the individual material surfaces are vertically interpolated back to standard pres-
 195 sure levels through FV’s so-called “REMAP” algorithm. This is needed because the La-
 196 grangian surfaces that vertically bound the finite volumes will eventually deform, neg-
 197 atively impacting the accuracy of the horizontal-to-Lagrangian-surface transport and the
 198 computation of the pressure-gradient terms.

199 There are various user-defined parameters and decisions that are made within the
 200 remapping algorithm. In its current implementation this involves 1) fitting piecewise parabolic
 201 (hereafter PPM) functions to input layer-mean values of T , u , v , q and tracers; 2) cal-
 202 culating PPM functions to output layer edges; and 3) integrating PPM functions between
 203 output layer edges to produce new layer-mean values of T , u , v , q and tracers. Note that
 204 T , u , v , q , C_p , K and Φ correspond to temperature, zonal wind, meridional wind, spe-
 205 cific humidity, specific heat capacity and kinetic and potential energy, respectively. This
 206 implementation setup is consistent with what is currently being used in most recent model
 207 versions (i.e. blue and green lines, Figure 1) and hereafter is referred to as REMAP Op-
 208 tion 2 (Table 1, left).

209 The alternative version – which best mimics what was used in MERRA-2 – involves
 210 two main changes to this procedure and is hereafter referred to as REMAP Option 1 (Ta-
 211 ble 1, right; red line in Figure 1). First steps 1) and 3) are performed only for u , v , q and
 212 tracers (not T). Second, three additional steps after 3) are added, the first two of which
 213 involve calculating total energy (TE) at input mid-layer pressures and then performing
 214 cubic interpolation and a posteriori integral conservation at output mid-layer pressures.
 215 Finally, temperatures are “remapped” from total energy via $T = (TE - K - \Phi)/C_p$.

216 When examining Table 1, it is important to note that Options 1 and 2 differ in two
 217 main respects. Of these, we find that the simulated ages are most sensitive to the inter-
 218 polation that occurs within step 5 in REMAP Option 1 (Table 1). The use of TE (as
 219 opposed to T), by comparison, is less consequential (Appendix A, Figure A1, left). To

Table 1. Finite Volume Remapping Algorithm: The two versions examined in this study control how individual material surfaces are vertically interpolated back to standard pressure levels. REMAP Options 2 and 1 corresponds to the configurations used in more recent (green and blue lines, Figure 1) and older (red and black lines, Figure 1) model configurations, respectively. Here T , u , v , C_p , K and Φ correspond to temperature, zonal wind, meridional wind, specific heat of air at constant pressure and kinetic and potential energy, respectively.

Step	REMAP Option 2 (CTRL)	REMAP Option 1 (MERRA-2)
1	Fit PPM functions to input layer-mean T , u , v , q and tracers	Fit PPM functions to input layer-mean u , v , q and tracers
2	Calculate PPM to output layer edges	Calculate PPM to output layer edges
3	Integrate PPM functions between output layer edges to produce new layer-mean T , u , v , q and tracers	Integrate PPM functions between output layer edges to produce new layer-mean u , v , q and tracers
4	n/a	Calculate $TE = C_p T + K + \Phi$ at input mid-layer pressures
5	n/a	Calculate TE at output mid-layer pressures using cubic interpolation and a-posteriori integral conservation
6	n/a	Construct “remapped” T via $T = (TE - K - \Phi)/C_p$

220 this end, the sensitivity experiments discussed in the next section mainly focus on identifying the age sensitivities in response to changes in the interpolation scheme used in REMAP
 221 Option 1, not to differences between the use of TE versus T .
 222

223 Finally, it is worth noting other important model development changes that occurred
 224 related to the parameterization of deep convection (Grell and Freitas (2014); Freitas et
 225 al. (2018)) which could, potentially, have an indirect impact on the stratospheric circulation
 226 through their influence on wave generation in the troposphere. As we show, however,
 227 while these have a substantial impacts upon their incorporation in a nonhydrostatic
 228 version of the model on characteristics like the diurnal cycle of precipitation (Arnold et
 229 al. (2020)) and on convective transport within the troposphere (Freitas et al. (2020)),
 230 their indirect influence on the stratosphere is less impactful.

231 2.2 Model Experiments

232 In order to investigate the drivers of the differences illustrated in Figure 1 we per-
 233 form targeted model experiments aimed at further disentangling the influence of recent
 234 model development changes on stratospheric transport properties (Table 2). First, we
 235 begin by defining a control experiment (CTRL; Table 2, row 1), which best corresponds
 236 to the blue line shown in Figure 1. Then we define three new experiments based off this
 237 control that are used to distinguish between the age changes resulting from changes in
 238 radiation versus changes in the handling of the REMAP algorithm (Section 3.2.1).

239 Specifically, these include experiments in which we revert back from RRTMG to
 240 Chou and Suarez (1994) in the shortwave (CSRAD; Table 2, row 2), b) revert back to
 241 the MERRA-2 REMAP approach (i.e. REMAP Option 1) (M2REMAP; Table 2, row
 242 3) and c) combine these two changes (CSRAD+M2REMAP; Table 2, row 4). Note that
 243 we have also have performed experiments in which RRTMG is reverted back to Chou

Table 2. GEOS Model Experiments: Targeted GEOS-5 model experiments based off a control experiment (row 1) were carried out to identify the influence of radiation (row 2) and the FV remapping algorithm changes since MERRA-2 (row 3), as well as their combined influence (row 4). Sensitivities within the FV remapping algorithm were further explored with respect to the order of the interpolation scheme used to calculate TE at output mid-layer pressure levels (rows 5-7). Experiments in rows 1-4 are 30-year-long AMIPs, whereas rows 5-7 refer to 30-member 3-month-long (DJF) EMIP experiments. Both AMIPs and EMIPs are used for climate statistic evaluation (see Appendix A for more on the correspondence between the two). By comparison, rows 8-9 refer to 1-year-long DAS runs used for evaluation of the analysis state.

Experiment Name	Configuration Change	Experiment Type
CTRL	Control, REMAP Option 2	AMIP (30 yrs.)
CSRAD	Chou-Suarez (1994) Shortwave (SW) Radiation	AMIP (30 yrs.)
M2REMAP	MERRA-2 REMAP Option 1 (cubic)	AMIP (30 yrs.)
CSRAD+M2REMAP	Chou-Suarez (1994) SW + REMAP Option 1 (cubic)	AMIP (30 yrs.)
LINEAR	MERRA-2 REMAP Option 1 (linear)	EMIP (30 members)
QUADRATIC	MERRA-2 REMAP Option 1 (quadratic)	EMIP (30 members)
CUBIC	MERRA-2 REMAP Option 1 (cubic)	EMIP (30 members)
CTRL-DAS	Control, REMAP Option 2	DAS (1 yr.)
CUBIC-DAS	MERRA-2 REMAP Option 1 (cubic)	DAS (1 yr.)

244 (1990) in the longwave, but these changes are less impactful, compared to the shortwave
245 radiation changes (not shown).

246 As shown in Section 3.2.1, the M2REMAP experiment produces the largest changes
247 in age-of-air, compared to the altered radiation experiments. To this end, we focus the
248 remainder of our investigation (Section 3.2.2) on examining a clean set of experiments
249 that distinguishes the impact of REMAP Option 1 versus Option 2 on simulated trans-
250 port. In particular, we perform three sensitivity experiments that differ from each other
251 only in terms of the calculation of TE at the mid-layer pressure levels, which we perform
252 using a linear (LINEAR; Table 2, row 5), quadratic (QUADRATIC; Table 2, row 6) and
253 cubic interpolation (CUBIC; Table 2, row 7) scheme, with the latter corresponding to
254 the approach that was used in MERRA-2. Note that, while the LINEAR and QUADRATIC
255 experiments do not actually correspond to any of the development tags shown in Fig-
256 ure 1, they highlight the large sensitivity of the mean age to changes in the interpola-
257 tion scheme that may otherwise seem innocuous. They also provide further evidence of
258 the strong influence of tropical lower stratospheric upwelling strength on stratospheric
259 mean age in GEOS.

260 Finally, in all experiments using REMAP Option 1 (i.e. M2REMAP, CSRAD+
261 M2REMAP, LINEAR, QUADRATIC, CUBIC) additional modifications to the diver-
262 gence damping coefficients were used so as to best ensure consistency with what was used
263 in MERRA-2. Specifically, these include changes to the number of layers for vertical sub-
264 grid mixing, the DAS coefficient for barotropic mode damping, the use of 2nd vs. 6th or-
265 der divergence damping and the strength of the divergence damping coefficients.

266

2.3 Analysis Approach

267

2.3.1 Stratospheric Circulation and Transport Diagnostics

268

269

270

271

272

273

274

275

276

277

278

279

280

281

282

To diagnose the transport circulation we focus primarily on the age-of-air (Hall and Plumb (1994)). This is inferred from an idealized global “clock” or ideal age tracer (Γ) (Thiele and Sarmiento (1990)) that is defined with respect to all grid points in the first model level. Initially, the ideal age tracer is set to zero throughout the troposphere and thereafter held to zero over the entire Earth’s surface, subject to a constant aging of 1 year/year throughout the atmosphere. We present here the statistically stationary (equilibrated) value of $\Gamma(r)$, which is equal to the average time since the air at a location r in the stratosphere last contacted the Earth’s surface. In addition to the mean age, we also show results from an idealized e90 tracer that is uniformly emitted over the entire surface layer and decays exponentially at a rate of 90 days⁻¹ such that concentrations greater than 125 ppb and less than 50 ppb tend to reside in the lower troposphere and stratosphere, respectively (Prather et al. (2011)). As this tracer features strong near-tropopause gradients and takes significantly less time to equilibrate, compared to the mean age, it is useful for evaluating stratosphere-troposphere-exchange and transport within the upper troposphere/lower stratosphere (Abalos et al. (2017, 2020); Orbe et al. (2020)).

283

284

285

286

287

288

289

In addition to the idealized tracers, we also evaluate the impacts of the age changes on real trace gas distributions. Two of the experiments shown here were run with full interactive chemistry and correspond to the two CCM1 (Phase 1 and Phase 2) integrations (red and green lines, Figure 1), which both employed the same Global Modeling Initiative (GMI) chemical mechanism (Strahan et al. (2013)). Results from these experiments show the imprint of the age-of-air changes on nitrous oxide (N₂O) and methane (CH₄).

290

291

292

293

294

295

296

297

298

299

300

As we show in Section 3, the changes in age-of-air across the different model versions are strongly tethered to changes in the advective component of the circulation, which we quantify using the Transformed Eulerian Mean (TEM) estimate of the Lagrangian transport of mass by the circulation. Thus, in addition to more standard Eulerian metrics of the circulation (e.g., zonal winds and temperatures), we focus on the vertical component of the TEM residual velocity, defined as $\bar{w}^* = \bar{w} + \frac{\partial(\psi \cos \phi)}{\partial \phi \partial p}$, where $\psi = \overline{v'\theta'}/\frac{\partial \theta}{\partial p}$ is the eddy stream function, θ refers to potential temperature and overbars and primes denote zonal means and deviations therefrom, respectively (Andrews et al. (1987)). In addition, we interpret the behavior in w^* using the Eliassen-Palm flux divergence ($\nabla \cdot \mathbf{F}$), whose horizontal ($\mathbf{F}(\phi)$) and vertical ($\mathbf{F}(p)$) components are respectively defined as $\mathbf{F}(\phi) = \text{acos}\phi[\frac{\partial u}{\partial p}\psi - \overline{u'v'}]$ and $\mathbf{F}(p) = \text{acos}\phi([f - \frac{\partial u \cos \phi}{\partial \phi \partial p}]\psi - \overline{u'\omega'})$.

301

2.3.2 Experimental Setup

302

303

304

305

306

307

We begin our analysis by interpreting the results shown in Figure 1, which are all based on historical AMIPs that were performed at the same cubed sphere C180 (approximately half-degree) horizontal resolution. As they represent more “official” model versions they serve as an important motivation for the experiments that follow. However, a clean/meaningful analysis of this set of runs is nonetheless hampered by the structural model differences between them.

308

309

310

311

312

313

314

315

Given the limitations of the experiments highlighted in Figure 1, we focus the bulk of our analysis on the model configurations listed in Table 2. For a subset of these model runs (rows 1-4) climatological AMIPs were carried at a C180 resolution and used to infer the climate characteristics of the different model configurations. For the other experiments (Table 2, rows 5-7) so-called “EMIPs” – ensembles of 3-month-long integrations initialized on approximately November 15 of each year between 1985 and 2015 – were performed. EMIPs for these experiments were performed at both C180 and C360 resolutions in order to examine the sensitivity of our results to changes in horizontal res-

316 olution. All of the experiments listed in Table 2 were integrated using the same ideal-
 317 ized passive tracer package (including the e90 and Γ tracers) described in Orbe et al. (2017).

318 As shown in Appendix B, comparisons of the the December-January-February (DJF)
 319 vertical profile of w^* , averaged over 1985-2015 and between the tropical turnaround lat-
 320 itudes, show excellent agreement between EMIP and AMIP integrations carried out us-
 321 ing the same model configuration (Appendix Figure B1). This somewhat incidental re-
 322 sult, represents, to the best of our knowledge, the first time that EMIP-based statistics
 323 have been shown to converge well to those from AMIPs for the stratospheric metrics con-
 324 sidered in this study. This suggests that EMIPs may provide a computationally more
 325 efficient alternative to AMIPs for use in quickly ascertaining the impacts of model changes.
 326 We note, however, that this approach is not appropriate for evaluating the time-integrated
 327 transport characteristics reflected in the age-of-air. To this end, we show results from
 328 both AMIP and EMIP experiments.

329 Finally, in addition to examining the climate statistics of the different model con-
 330 figurations we also inquire into implications for the analyzed atmospheric states from data
 331 assimilation for a subset of the experiments (Table 2, rows 8-9). Specifically, we exam-
 332 ine the root-mean-square error of various climate fields (**Amal, need description of rel-**
 333 **evant metrics/analysis**). This evaluation is important given that in GEOS-R21C any un-
 334 derlying model biases will be partly ameliorated through replaying of the model state
 335 to the analysis. Assessing the impact of reduced biases from the free-running model for
 336 the analysis state is therefore important for informing the development of GEOS-R21C.

337 2.4 Observations and Reanalyses

338 While our focus is on interpreting and understanding the different model config-
 339 urations, we incorporate observations to provide context when possible, although we do
 340 not present an exhaustive evaluation of the model’s transport characteristics (for that
 341 see earlier studies including Orbe et al. (2017, 2018)). However, as the tracers are not
 342 directly integrated in MERRA-2 (with the exception of ozone), we compare against in-
 343 dependent observational estimates. For the mean age we first compare simulated merid-
 344 ional age profiles at 50 hPa with values derived from in situ aircraft measurements of car-
 345 bon dioxide (CO_2), averaged in 2.5 degree latitude bins over the altitude range 19.5 to
 346 21.5 km (Boering et al. (1996), see also Figure 5 in Hall et al. (1999)).

347 We also briefly evaluate impacts of transport biases on the simulated trace gas dis-
 348 tributions for the CCM1 Phase 1 and 2 experiments. The simulated fields of methane
 349 (CH_4) are compared with the climatologies derived for 1991–2002 from the Halogen Oc-
 350 cultation Experiment (HALOE) on board the Upper Atmosphere Research Satellite (UARS)
 351 (Grooß and Russell III (2005)). Comparisons of simulated nitrous oxide (N_2O) are made
 352 against 2005–2015 climatologies derived from the Microwave Limb Sounder (MLS) on
 353 the Earth Observing System (EOS) Aura satellite. We use the 190-GHz retrieval from
 354 Version 4.2 because the 640-GHz data set ends in summer 2013 due to the failure of the
 355 N_2O primary band.

356 For the circulation diagnostics nearly all comparisons are made relative to MERRA-
 357 2 and comparisons against ERA-5 (not shown) reveal a similar picture. One exception,
 358 however, is the vertical component of the TEM circulation (w^*), which shows some dif-
 359 ferences in vertical structure between MERRA-2 and a 30-member ensemble of (free-running)
 360 AMIP integrations produced using the MERRA-2 model, hereafter referred to as MA2AMIP
 361 (Collow et al., 2017)(Appendix Figure A1, right). This difference in vertical structure
 362 may reflect differences in the vertical levels used to calculate the (highly derived) TEM
 363 circulation, which is notoriously sensitive not only to differences in the formulation of
 364 the equations (Hardiman et al., 2010), but also to the vertical resolution of the input ve-
 365 locities and associated heat and momentum fluxes that are used to calculate the verti-
 366 cal derivatives in the eddy stream function (Gerber & Manzini, 2016). Regardless of the

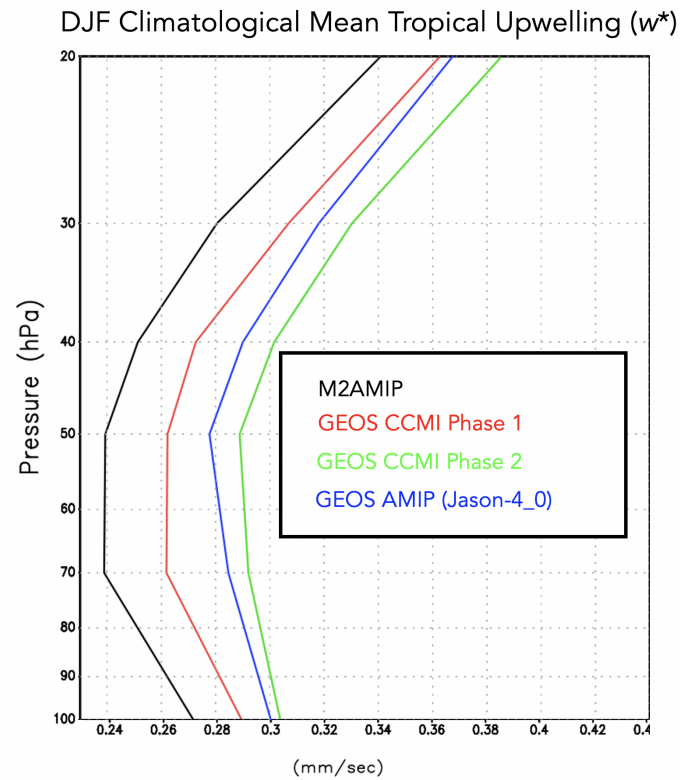


Figure 2. The DJF 1985-1994 climatological mean vertical residual mean velocity, w^* , averaged between the turnaround latitudes for GEOS model configurations corresponding to the CCM1 Phase 1 (red) and Phase 2 (green) submissions and to Jason 4.0 GEOS AMIP (blue). M2AMIP is shown in black.

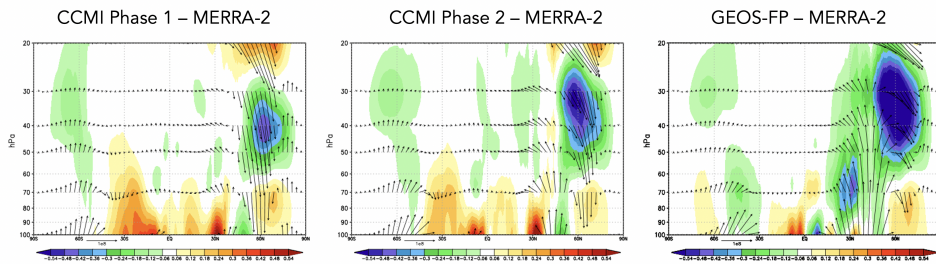
DJF Climatological Mean Eliassen-Palm Flux Divergence ($\nabla \cdot \mathbf{F}$)

Figure 3. Colors show anomalies in the DJF climatological mean Eliassen-Palm (EP) flux divergence between the CCMI Phase 1 (left), CCMI Phase 2 (middle) and Jason 4.0 GEOS AMIP (right) model versions, relative to MERRA-2. Arrows denote anomalies in the vertical and meridional EP flux vectors (relative to MERRA-2).

367 reason, it is essential that comparisons of the simulated TEM velocities be made using
 368 consistent calculations; therefore, when comparing the TEM circulation in the A(E)MIPS,
 369 in lieu of MERRA-2 we use results from M2AMIP. This ensures as apples-to-apples compar-
 370 ison of the TEM in the various GEOS experiments with the MERRA-2 system as possi-
 371 ble (note that for non-derived measures (i.e., winds, temperatures) the raw MERRA-
 372 2 output is used).

373 3 Results

374 3.1 Reduction in Stratospheric Mean Age Since MERRA-2

375 We begin by interpreting the reduction in mean age exhibited in more recent model
 376 versions in terms of changes in the strength of upwelling in the tropical lower stratosphere.
 377 In particular, the reductions in Γ (Figure 1) are consistent with increases in the strength
 378 of lower stratospheric tropical upwelling, with w^* becoming progressively stronger in more
 379 recent model tags, relative to MERRA-2 (Figure 2). Though perhaps naive, this rela-
 380 tionship between lower stratospheric upwelling and the mean age is consistent with the
 381 long-term behavior of Γ inferred from both historical and projected future climate simu-
 382 lations (Butchart et al. (2010); Abalos et al. (2021)). A strong relationship between the
 383 strength of lower stratospheric ascent and the mean age was also shown to hold in the
 384 CCMVal models (see Fig. 5.20 in J. Neu et al. (2010)). Nevertheless, it is important to
 385 note that a clear relationship between w^* and Γ is not a priori expected, as the age-of-
 386 air is also known to be very sensitive to mixing, which may be important in interpret-
 387 ing differences among the CCMI Phase 1 models (Dietmüller et al. (2018)).

388 The differences in w^* highlighted in Figure 2 are associated with enhanced Eliassen-
 389 Palm flux convergence over NH midlatitudes (Figure 3). Increased wave convergence is
 390 evident not only within the subtropical lower stratosphere ($< 30^\circ\text{N}$, 50-100 hPa) but also
 391 over higher latitudes and altitudes ($\sim 40^\circ\text{-}70^\circ\text{N}$, 20-50 hPa). The fact that differences
 392 in extratropical wave convergence imprint on tropical upwelling is consistent with our
 393 understanding of the so-called “downward control” principal (Haynes et al. (1991)). In
 394 particular, the strength of the residual mean streamfunction (Ψ^*) is, via downward con-
 395 trol, directly related to the vertically integrated eddy-induced total zonal force above that
 396 level and has contributions both from the (resolved wave) Eliassen-Palm flux divergence
 397 (Figure 3) as well as parameterized waves (not shown). The tropical upward mass flux

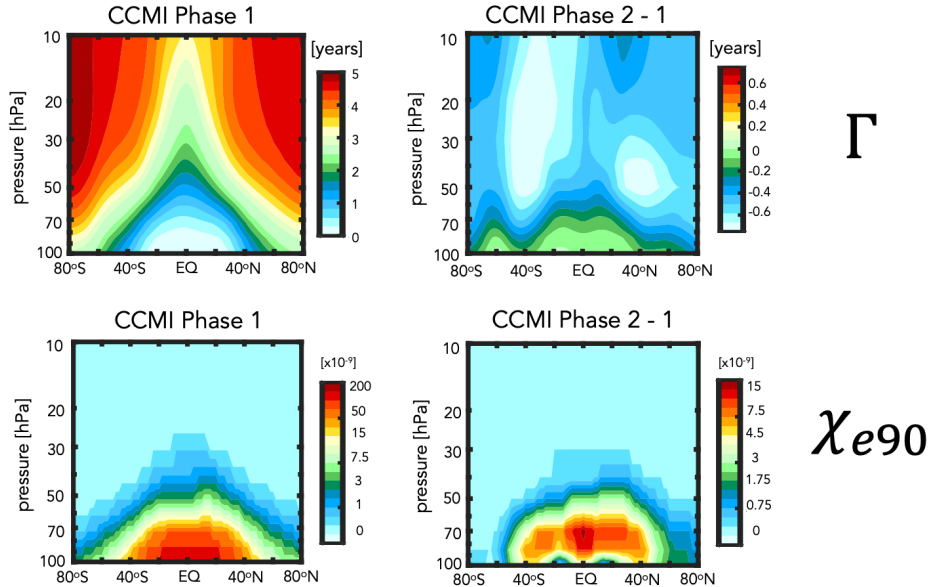


Figure 4. The climatological mean (2000-2010) distribution of the mean age-of-air (Γ) (left, top) and e90 idealized tracers (left, bottom) for the CCMI Phase 1 model configuration. Climatological differences between the CCMI Phase 2 and Phase 1 model configurations are shown in the left panels. Note that a nonlinear colorbar has been used in the e90 subplots.

398 – defined as $\Psi_{\max}^* - \Psi_{\min}^*$ evaluated at the turnaround latitudes (e.g. Rosenlof (1995)) –
 399 is therefore directly dependent on the wave forcing aloft.

400 While the reduction in Γ (Figure 1) of $\sim 30\%$ at 50 hPa is significant, it is neither
 401 clear if this change is representative of other altitudes within the stratosphere nor how
 402 this age bias imprints on real chemical species. To this end, we begin by comparing the
 403 full latitude-pressure distribution of changes in Γ and another passive tracer (e90) (Fig-
 404 ure 4) between the CCMI Phase 1 and Phase 2 model configurations (red and green lines,
 405 Figure 1). In particular, we find that the changes in both passive tracers – large reduc-
 406 tions in Γ within both hemispheres (Fig. 4, top right) and increased values of e90 within
 407 the lower stratosphere (Fig. 4, bottom right) – are reflective of an overall increase in the
 408 strength of the transport circulation. This is highlighted in the CCMI Phase 2 – 1 model
 409 differences for the passive tracer distributions (Fig. 4, right panels) which are shown in
 410 the absence of robust observational constraints of Γ at higher altitudes (or any obser-
 411 vational constraints for e90, for that matter). The reduced/increased stratospheric bur-
 412 dens of the age and e90 tracers are consistent with stronger upwelling in the CCMI Phase
 413 2 model configuration (Figure 2).

414 While the observational constraints on Γ presented in Figure 1 and the departure
 415 of w^* away from MERRA-2 suggest that transport properties of the newer model con-
 416 figurations are moving in the wrong direction, it is relevant to ask whether or not the
 417 trace gas satellite measurements also support this conclusion. Indeed, comparisons with
 418 observations show larger biases in N_2O (Fig. 5, top panels) and CH_4 (Fig. 5, bottom pan-
 419 els), increasing from 10% to 30% in the CCMI Phase 2 model configuration, depending
 420 on the species. The patterns of these biases are generally consistent with the biases in
 421 the mean age (Fig. 4), suggesting a strong link between the tracers. Recall that the same
 422 chemistry mechanism is used in both CCMI Phase 1 and 2 simulations.

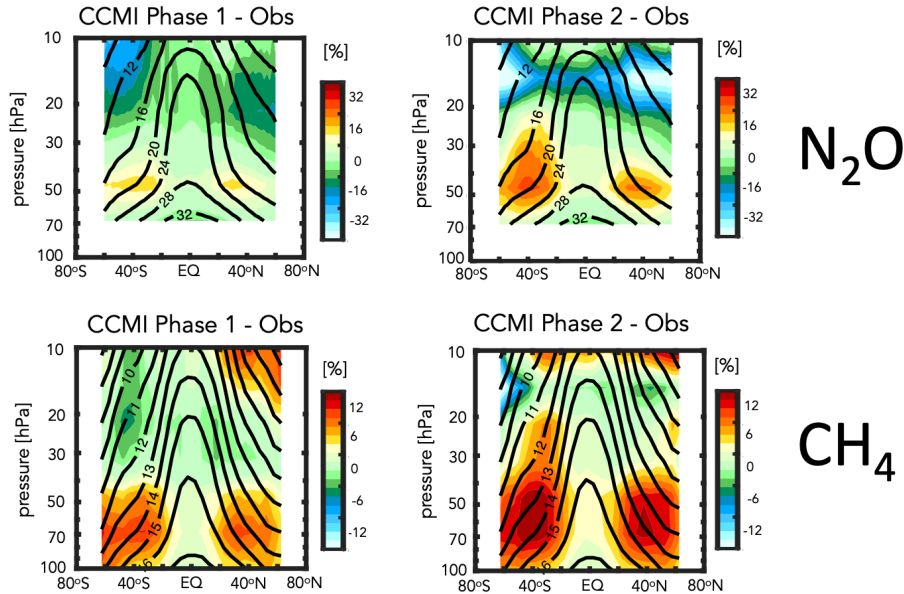


Figure 5. Colors shown anomalies in the simulated distributions of nitrous oxide (N_2O) (top) and methane (CH_4) (bottom), relative to the MLS and HALOE observed values, respectively, for the CCMI Phase 1 (left) and Phase 2 (right) GEOS model configurations. Climatological mean observed values are shown in the black contours.

423 The fact that the mean age changes have a significant imprint on the simulated trace
 424 gases is consequential for the GEOS-RC21 system. However, the configurations shown
 425 in Fig. 1-5 differ in many respects (physics, resolution, radiation, FV remapping algo-
 426 rithm) and it is difficult to meaningfully interpret what is driving the changes in w^* (and
 427 the tracers). We therefore move next to the targeted model experiments (Table 2) in or-
 428 der to interpret the model development steps that resulted in these transport circula-
 429 tion changes.

430 3.2 Identifying Drivers of Upwelling and Tracer Changes Since 431 MERRA-2

432 3.2.1 Radiation versus REMAP Algorithm

433 As discussed in Section 2, among the model changes that were made since MERRA-
 434 2, the changes in radiation and the FV remapping algorithm are most likely to directly
 435 have impacted the stratospheric circulation. We therefore begin by assessing which of
 436 these changes dominates the decreases in Γ shown in Figure 1.

437 Figure 6 shows the distribution of Γ for experiments in which the shortwave radi-
 438 ation and REMAP updates since MERRA-2 have successively been undone. Relative to
 439 the control experiment (CTRL; Table 2, row 1), the reversion back to Chou (1992) in
 440 the shortwave results in an increase in the mean age of ~ 0.5 years throughout the strato-
 441 sphere (CSRAD; Table 2, row 2). Though significant, this change in Γ is smaller than
 442 the change that results from reverting back to REMAP Option 1 (M2REMAP; Table
 443 1; row 3), in which the mean age increases by ~ 1 year. The combined impacts of both
 444 changes (CSRAD+M2REMAP; Table 1 row 4) is roughly linear, with age values of \sim
 445 5.5 years over high latitudes at 50 hPa, consistent with the values simulated by the GEOS-

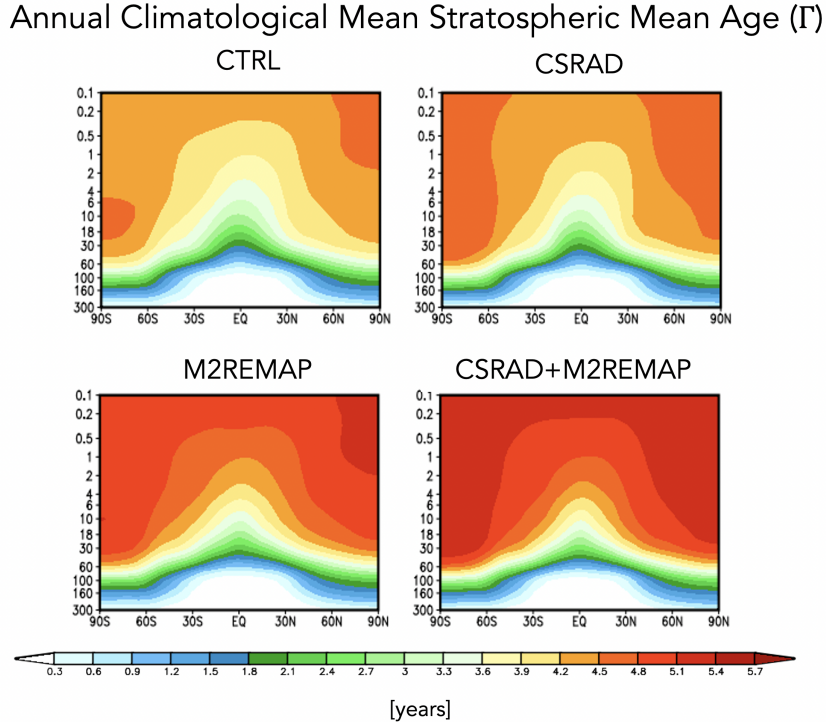


Figure 6. Colors show the simulated 2000-2010 climatological annual mean distributions of the mean age-of-air (Γ) for the CTRL (top left; Table 1, row 1), CSRAD (top right; Table 1, row 2), M2REMAP (bottom left; Table 1, row 3) and combined CSRAD+M2REMAP (bottom right; Table 1, row 4) experiments.

446 CTM MERRA-2 integration (black line, Figure 1) and with the CCM1 Phase-1 version
447 of the model (red line, Figure 1).

448 Next we ask if the behavior of Γ exhibited in Figure 6 can be interpreted in terms
449 of changes in the strength of lower stratospheric tropical upwelling and extratropical wave
450 convergence, as our previous analysis of the CCM1 experiments suggested. Indeed, Fig-
451 ure 7 shows that values of upwelling decrease in the CSRAD and M2REMAP experiments,
452 relative to the CTRL integration. The increase in upwelling resulting from both changes
453 (CSRAD+M2REMAP) is still larger, consistent with the larger age decreases in that ex-
454 periment. This change in the behavior of w^* within the tropical stratosphere can be in-
455 terpreted in terms of changes in the Eliassen Palm flux convergence over NH midlati-
456 tudes (not shown), which features smaller values in the CSRAD, M2REMAP (and CSRAD+
457 noindentMSREMAP) experiments. Note that our examination of the changes in
458 w^* are derived from EMIP integrations, which we showed previously converge (for DJF)
459 to the statistics derived from corresponding AMIP experiments.

460 3.2.2 FV REMAP Algorithm: Sensitivity of Climate Statistics

461 Having shown in the previous section that the largest changes in the mean age were
462 realized through the reversion back to REMAP Option 1, we now investigate further the
463 sensitivity of the transport circulation to the choice of remapping interpolation scheme.
464 In particular, we compare simulations in which total energy is calculated at new mid-
465 layer pressures using cubic, quadratic and linear interpolation prior to the aposterior in-
466 tegral conservation (Table 2, rows 5-7). In addition, in this section we seek to understand

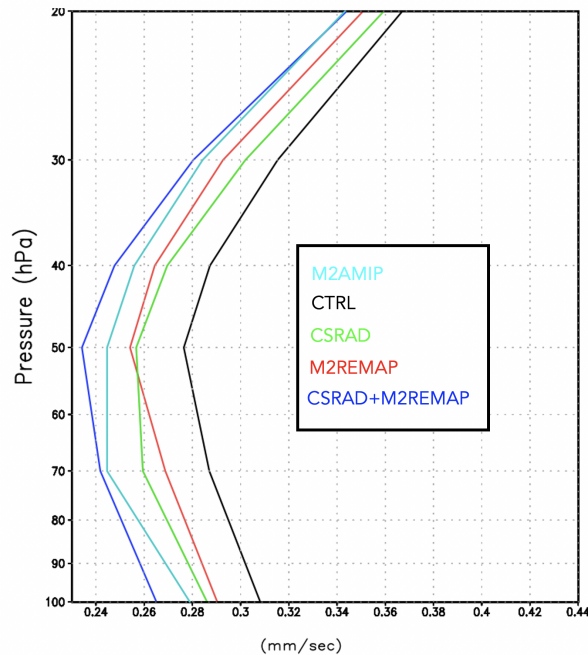
DJF Climatological Mean Tropical Upwelling (w^*)

Figure 7. The DJF climatological mean vertical residual mean velocity, w^* , averaged between the turnaround latitudes for the CTRL (red line; Table 2, row 1), CSRAD (green line; Table 2, row 2), M2REMAP (blue line; Table 2, row 3) and combined CSRAD+M2REMAP (cyan line; Table 2, row 4) experiments. M2AMIP is shown in black. **REORDER COLORS**

467 how the changes in the Eliassen-Palm flux convergence over NH midlatitudes arise via
 468 analysis of the large-scale wind structure.

469 Figure 8 (left panels) shows a clear sensitivity in tropical upwelling to the choice
 470 of interpolation scheme, with w^* progressively increasing in strength moving from the
 471 CUBIC to QUADRATIC to LINEAR schemes. This sensitivity is robust across horizon-
 472 tal resolutions as the same suite of experiments performed at C360 exhibit the same sensi-
 473 tivity (Fig. 8, right panels). While no current model tag actually employs a linear scheme,
 474 this suite of experiments highlights the strong sensitivity to choice of interpolation scheme
 475 within the remapping algorithm; to the best of our knowledge, this result has not been
 476 reported in the literature. Furthermore, as we show next, this clean set of experiments
 477 allow us to inquire mechanistically into the processes that are driving the changes in wave
 478 convergence over midlatitudes, unencumbered by differences in horizontal resolution, physics,
 479 etc.

480 Consistent with our expectations based on the analysis of the previous experiments,
 481 the drivers of the changes in w^* are related to increased wave convergence moving from
 482 the CUBIC to QUADRATIC to LINEAR schemes (Figure 9). Over extratropical lati-
 483 tudes, the zonal force associated with this enhanced wave convergence is associated with
 484 enhanced downwelling at high latitudes that, through mass balance, is accompanied by
 485 enhanced upwelling in the tropics. This indirect impact of higher latitude wave drag is
 486 evident in Appendix Figure B1, which show stronger upwelling/downwelling in LINEAR
 487 and QUADRATIC experiments over the tropics/polar region.

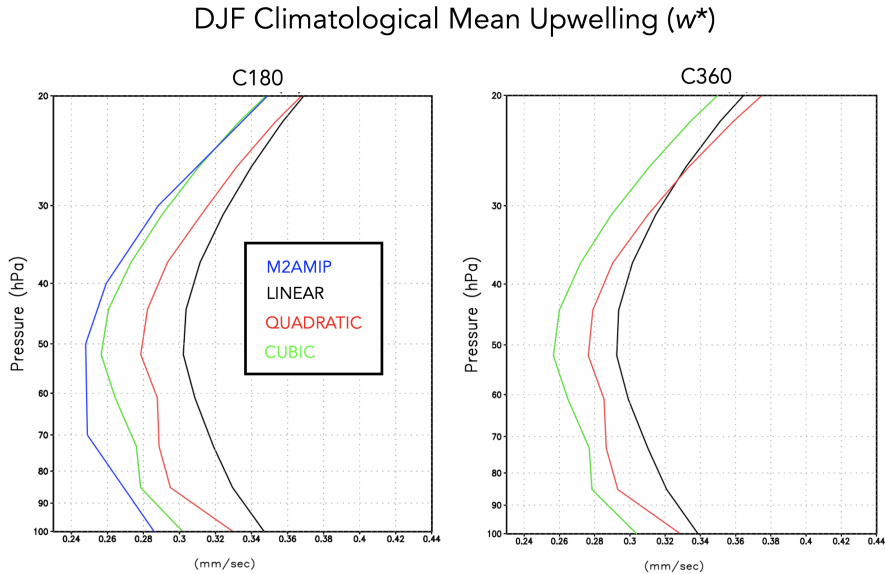


Figure 8. The DJF climatological mean vertical residual mean velocity, w^* , averaged between the turnaround latitudes for the CTRL (cyan line; Table 2, row 1), LINEAR (green line; Table 2, row 5), and QUADRATIC (blue line; Table 2, row 6) experiments. MERRA-2 is shown in black.

488 Next we exploit the fact that these experiments only differ with respect to the in-
 489 terpolation scheme in order inquire further into the drivers of the wave convergence changes.
 490 To this end, Figure 10 compares profiles of the zonal mean zonal wind between the CU-
 491 BIC, QUADRATIC and LINEAR experiments, averaged over the region of enhanced wave
 492 convergence (i.e. 20°N - 60°N). The experiments featuring stronger wave convergence (LIN-
 493 EAR and QUADRATIC) are also simulations with stronger zonal winds, relative to MERRA-
 494 2, especially above 70 hPa. This change in winds occurs at both C180 (Fig. 10, left panel)
 495 and C360 (Fig. 10, right panel) resolutions.

496 Structurally, the increase in zonal wind strength over northern extratropical mid-
 497 latitudes is reflective of a poleward shift in the zonal winds as the critical latitude, i.e.
 498 where the zonal wind is zero, shifts northward in the QUADRATIC and, especially, LIN-
 499 EAR integrations, relative to the CUBIC experiment (Figure 11). Since stationary waves
 500 only propagate in westerly zonal flow, the latitude where zonal flow is zero acts a bound-
 501 ary for wave propagation (Hardiman et al. (2014)). As a result, this shift in critical lat-
 502 itude results in enhanced wave propagation in that region.

503 Figures 10 and 11 highlight how the changes in zonal winds in the LINEAR and
 504 QUADRATIC experiments reflect a degradation in model skill, relative to MERRA-2,
 505 throughout the entire stratosphere. The changes in upwelling, mean age, chemical trace
 506 gases and zonal winds thus provide a coherent and self-consistent picture suggestive of
 507 a degradation in the representation of the stratospheric circulation since MERRA-2. That
 508 is, an increased bias in the stratospheric northern zonal winds are, via their influence on
 509 wave convergence, compromising changes in the strength of the mean meridional over-
 510 turning circulation and its impact on composition. It is interesting to note that the wind
 511 biases also extend into the troposphere and show degraded skill relative to MERRA-2
 512 in the LINEAR and QUADRATIC experiments (Figure 11). Examination of other fields
 513 (i.e. tropopause biases, Appendix Figure C1) present somewhat more of a nuanced story
 514 that depends more sensitively on latitude and season considered. The improvements in

DJF Climatological Mean Eliassen-Palm Flux Divergence ($\nabla \cdot \mathbf{F}$)

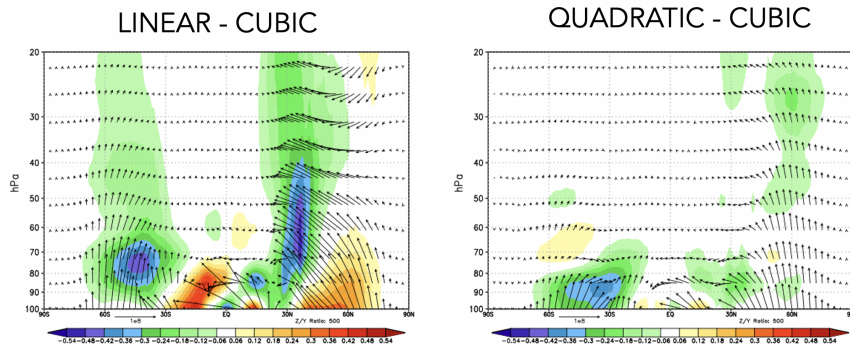


Figure 9. Colors shown anomalies in the DJF climatological mean Eliassen-Palm (EP) flux divergence in the LINEAR (left) and QUADRATIC (right) experiments, relative to the CUBIC model experiment. Arrows denote anomalies in the vertical and meridional EP flux vectors.

DJF Climatological Mean Zonal Wind (20°N-60°N)

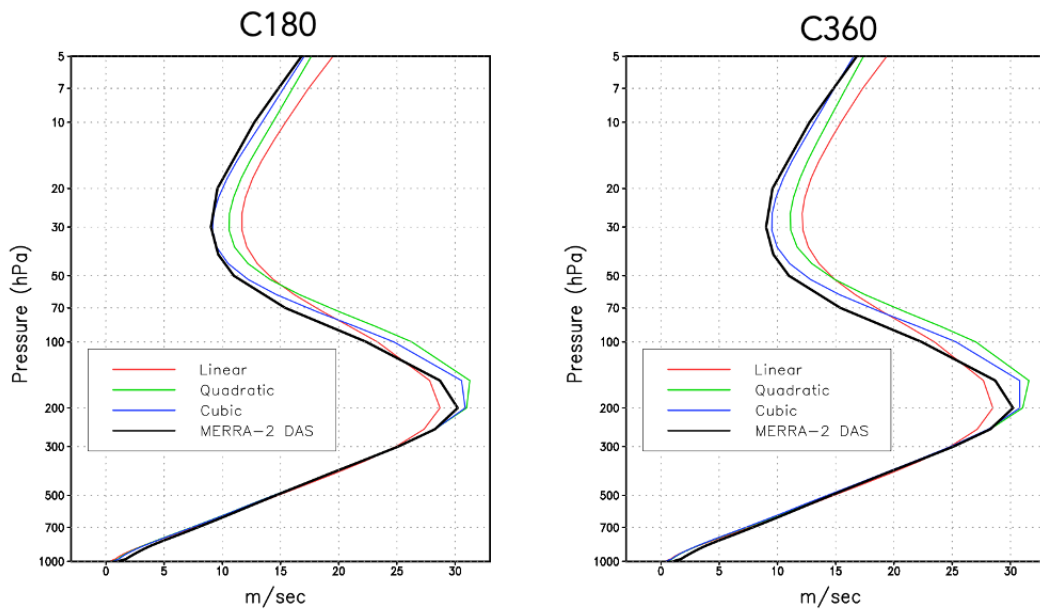


Figure 10. Vertical profiles of the DJF climatological mean zonal mean zonal winds in the LINEAR (red), QUADRATIC (green) and CUBIC (blue) experiments, averaged between 20°N and 40°N. MERRA-2 is shown in the black line. Results for both C180 (left) and C360 (right) experiments are provided.

DJF Climatological Zonal Mean Zonal Wind Anomalies Relative to MERRA-2

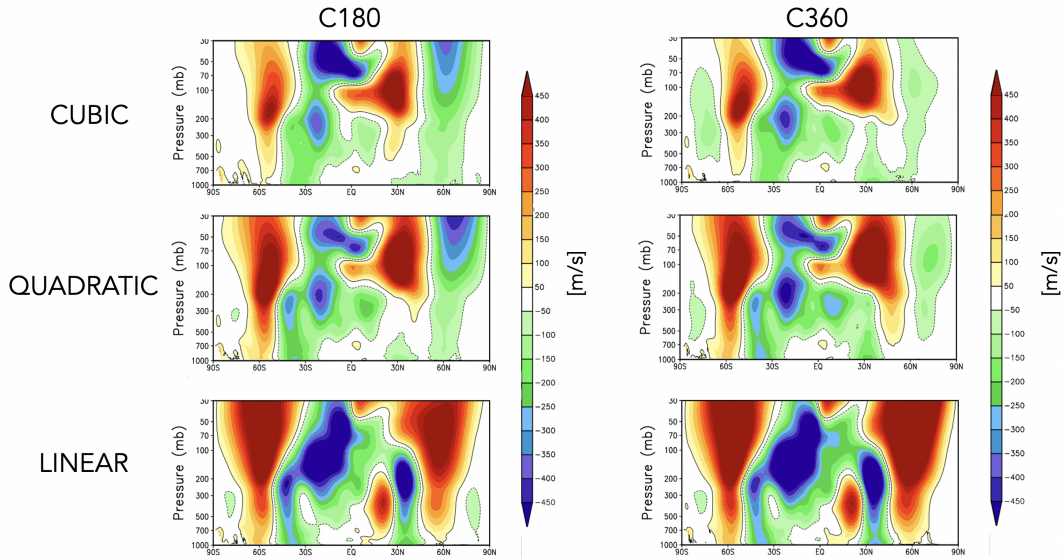


Figure 11. Colors shown anomalies in the DJF climatological mean zonal mean zonal winds in the CUBIC (top), QUADRATIC (middle) and LINEAR (bottom) experiments, relative to MERRA-2. Results for both C180 (left) and C360 (right) experiments are provided.

515 the zonal winds, however, are most relevant for setting the upwelling characteristics within
 516 the tropical lower stratosphere via their influence on wave propagation into that region.

517 Finally, to better understand why these impacts on the winds have such a conse-
 518 quence for the wave convergence properties within the stratosphere, next we examine the
 519 zonal structure of these biases in the middle stratosphere (Figure 12). This reveals that
 520 the enhanced winds in the LINEAR (and, to a lesser extent, QUADRATIC) integrations
 521 are concentrated over the North Pacific at both C180 (Fig. 12, left) and C360 (Fig. 12,
 522 right) resolutions (a similar picture emerges within the troposphere, not shown). As this
 523 region is the primary region dominating the stationary component of the upward flux
 524 of vertical wave activity (Plumb (1985), see their Figure 4) it is perhaps not surprising
 525 that this region is having a profound impact on the mean overturning circulation. Again,
 526 as with the zonal mean wind changes, the increases in wind strength over the North Pa-
 527 cific represent degraded model skill relative to MERRA-2. Note that comparisons with
 528 ERA-5 reveal a similar bias (not shown).

529 **3.2.3 FV REMAP Algorithm: Sensitivity of DAS Analysis State**

530 Up to this point our focus has been on evaluating the various model configurations
 531 via use of 30-year long AMIPs, which are required for deriving the integrated transport
 532 statistics (i.e. age-of-air) that reflect the long timescales relevant to setting the strato-
 533 spheric transport circulation. However, this not only poses practical challenges for model
 534 development purposes (which may be ameliorated, for some variables, through use of EMIPs),
 535 but it is also not obvious how the time-integrated model biases inferred from AMIPs man-
 536 ifest in a data assimilation (DAS) context. To this end, here we briefly comment on im-
 537 plications for the DAS analysis state.

DJF Climatological 30 hPa Zonal Wind Anomalies Relative to MERRA-2

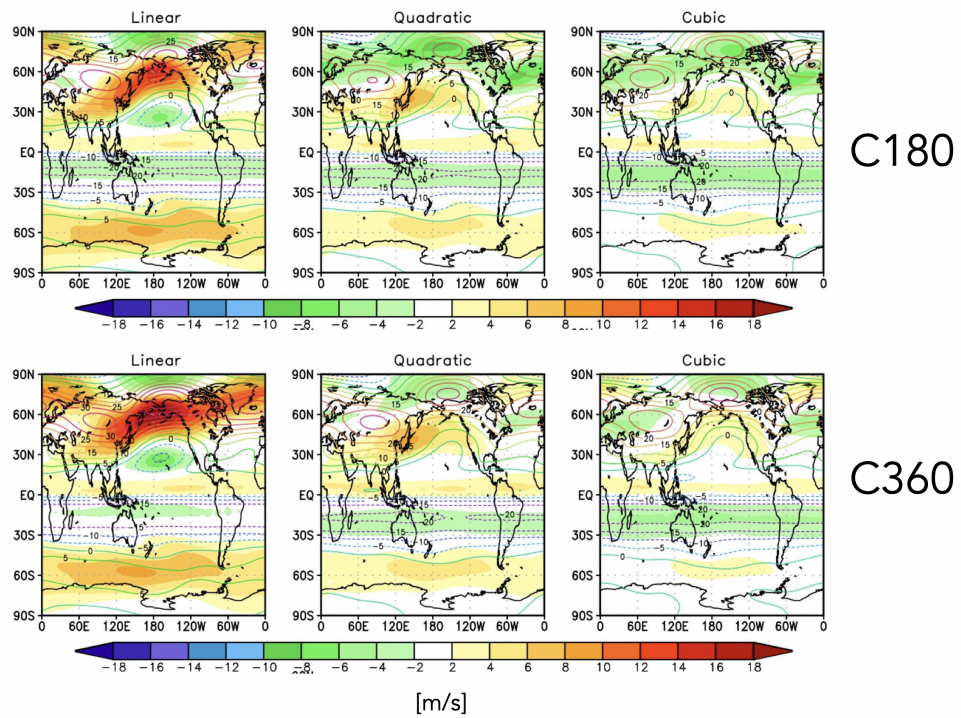


Figure 12. Colors shown anomalies in the DJF climatological mean zonal winds at 30 hPa in the CUBIC (right), QUADRATIC (middle) and LINEAR (left) experiments, relative to MERRA-2. Results for both C180 (top) and C360 (bottom) experiments are provided.

PLACEHOLDER

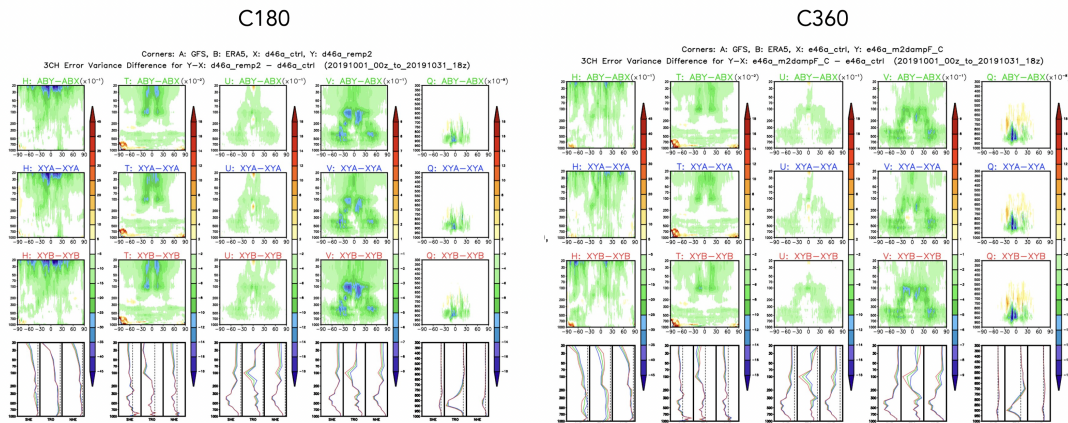


Figure 13. Need to fill in when figure has been decided.

538 In particular, we compare two DAS experiments one mimicking MERRA2 (d46aremp2)
 539 and one mimicking the control configuration (d46actrl) (Table 2, rows 8-9). As in the
 540 previous section, we also consider the robustness of results to changes in horizontal res-
 541 olution.

542 *Need to write when receive Amal's new figure (current Figure 13 is only a place-*
 543 *holder).*

544 4 Conclusions

545 Here we have presented an analysis aimed at understanding differences in the rep-
 546 resentation of the stratospheric circulation in recent candidate systems for GEOS-R21C,
 547 relative to older versions of GEOS-5 similar to that which was used to produce MERRA-
 548 2. Using targeted model experiments oriented at disentangling various model develop-
 549 ment updates, we have identified a key role played by changes in the remapping algo-
 550 rithm within the model's finite-volume dynamical core. Our key results are as follows:

551 #1. The stratospheric mean age-of-air in GEOS-5 is sensitive to the degree of the
 552 interpolation scheme that is used to calculate layer-mean values of total energy, u , v and
 553 tracers. Different treatment of the vertical remapping algorithm (REMAP Option 1 vs.
 554 2) result in mid-stratospheric (50 hPa) age-of-air differences of ~ 1 year over high lat-
 555 itudes, or about 30% climatological mean values.

556 #2. The age-of-air sensitivities reflect, to first order, changes in the strength of trop-
 557 ical upwelling associated with the Brewer-Dobson circulation which are in turn are driven
 558 by changes in EP flux convergence over northern midlatitudes. Changes in wave conver-
 559 gence reflect shifts in (critical lines of) wave propagation that originate in the troposphere
 560 over the Pacific Ocean, a region of strong upward wave activity.

561 #3. The degradation of age-of-air, upwelling and zonal wind climate statistics man-
 562 ifest in AMIPs, also translate to degradations in the DAS analysis states of a broad range
 563 of variables. These results are are not sensitive to horizontal resolution.

564 Although our focus here has been on the stratospheric transport circulation, mo-
 565 tivating our use of tracer-independent metrics like the age-of-air, our results have clear

566 implications for constituent transport in GEOS-R21C. In particular, we showed that the
 567 increased age-of-air biases correspond to increased biases in the representations of CH₄
 568 and N₂O moving from the CCM1 Phase 1 to Phase 2 model configuration. This com-
 569 ports with well-known correlations between the mean age and stratospheric trace gases,
 570 reinforcing the fact that model transport inaccuracies continue to significantly affect sim-
 571 ulations of important long-lived chemical species in the stratosphere (Hall et al. (1999)).

572 Our results highlight the key role played by model numerics in transport (e.g., Rood
 573 (1987)). The sensitivities in the age-of-air documented herein are also consistent in spirit
 574 with the findings in Gupta et al. (2020) who showed significant age differences occurring
 575 between spectral versus finite-volume numerics. Our results, however, suggest that there
 576 remain large sensitivities even within a given (FV) dynamical core. Furthermore, we also
 577 show that that statistics derived from long AMIPS also manifest within a data assim-
 578 ilation context, which raises important questions as to the degree to which model biases
 579 can be ameliorated through assimilation of observations.

580 Looking forward, our findings support and build on the recommendation proposed
 581 in Gupta et al. (2020) for the construction of dynamical core benchmark tests aimed at
 582 determining how underlying AGCM numerics impact climatological transport proper-
 583 ties. In particular, in addition to the age-of-air, the authors propose a range of strato-
 584 spheric circulation diagnostics that should be evaluated including the zonal mean zonal
 585 winds, eddy temperature variance and zonal spectra of eddy kinetic energy. Our anal-
 586 ysis reveals an important role to be played by the climatological zonal mean wind struc-
 587 ture as it impacts wave convergence over midlatitudes; we therefore also recommend ex-
 588 plicit consideration of the Eliassen Palm flux convergence and tropical upwelling (w^*)
 589 fields as they may be crucial for interpreting age-of-air changes.

590 One somewhat incidental – but practical - result from our analysis is that the statis-
 591 tics of $\nabla \cdot \mathbf{F}$ and w^* are well approximated by ensembles of so-called EMIP integrations.
 592 As these are substantially easier to run than AMIPs these could provide a “first pass”
 593 when evaluating new proposed model development changes, without the immediate need
 594 to integrate AMIP-style experiments. We emphasize, however, that this statement should
 595 only apply to a first stage in model development as the age-of-air will reflect the time
 596 integrated impacts of both advection and mixing.

597 Finally, we conclude by noting that, while we have focused on sensitivities within
 598 the FV remapping algorithm, our results have highlighted important sensitivities to changes
 599 in radiation and, to a lesser extent, changes in parameterized convection. Though not
 600 the dominant drivers of the age-of-air changes identified here, the former could poten-
 601 tially influence the age both directly through changes in thermal structure and indirectly
 602 by modifying wave propagation and/or generation in the troposphere. Future work will
 603 focus on examining these impacts.

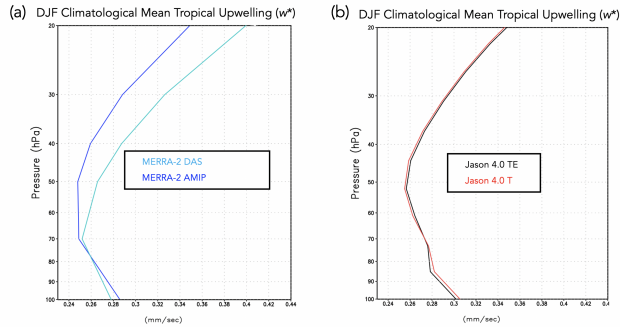


Figure A1. The DJF climatological mean vertical residual mean velocity, w^* , averaged between the turnaround latitudes compared between MERRA-2 (cyan) and the M2AMIP ensemble (blue) (left) and between two Jason 4.0 experiments remapping to T (red) versus TE (black) (right).

Appendix A Sensitivities in Calculation of TEM Upwelling

There are various aspects of the calculation of the TEM circulation that warrant further comment. First, the vertical component of the TEM circulation (w^*) shows some differences in vertical structure between MERRA-2 and the 30-member M2AMIP ensemble (Appendix Figure A1, left). This difference in vertical structure may reflect differences in the vertical levels used to calculate the (highly derived) TEM circulation. To this end, all comparisons of simulated TEM velocities in the AMIPs are made relative to M2AMIP, not MERRA-2. **UNSATISFYING EXPLANATION.**

Second, whereas the modeling experiments listed in Table 2 (rows 5-7) focus on the sensitivity of Step 5 in REMAP Option 1 to the choice of interpolation scheme, another difference between REMAP Options 1 and 2 is the use of TE versus T, respectively. To test the impact of this difference, we ran a new experiment (CUBIC-T) which is identical to the CUBIC experiment (Table 2, row 7), except that T is remapped from input layer mean pressure locations to standard output layer mean locations directly using cubic interpolation (i.e., no computation of TE or a-posteriori energy conservation applied). Appendix Figure A1 (right) shows that this has little impact on the strength of tropical upwelling, suggesting that the w^* differences between REMAP Options 1 and 2 are dominated by sensitivities to the choice of interpolation scheme, not the use of TE versus T.

Appendix B Correspondence between EMIP and AMIP w^*

Appendix Figure B1 shows the close correspondence in DJF climatological mean w^* , averaged between the turnaround latitudes, from AMIP and EMIP experiments using the CUBIC configuration.

Appendix C Changes in Tropical and High Latitude Upwelling

Appendix Figure C1 compares the behavior in residual mean upwelling among the LINEAR, QUADRATIC and CUBIC experiments over the latitudes between the (tropical) turnaround latitudes (left) and poleward of the northern turnaround latitude (right). The ordering among experiments in both regions reflects how increases in downwelling at high latitudes are, through mass balance, accompanied by enhanced upwelling in the tropics.

PLACEHOLDER

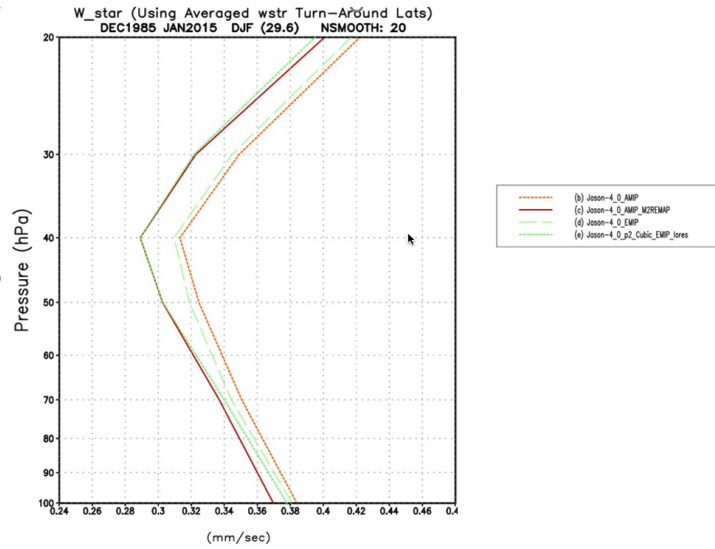


Figure B1. PLACEHOLDER FIGURE: The DJF climatological mean vertical residual mean velocity, w^* , averaged between the turnaround latitudes for the CTRL experiment (Table 2, row 1). Results based on a 30-year-long AMIP experiment (dotted orange line) and a 30-member ensemble of three-month-long EMIP experiments (dashed green line) are shown.

DJF Climatological Mean Upwelling (w^*)

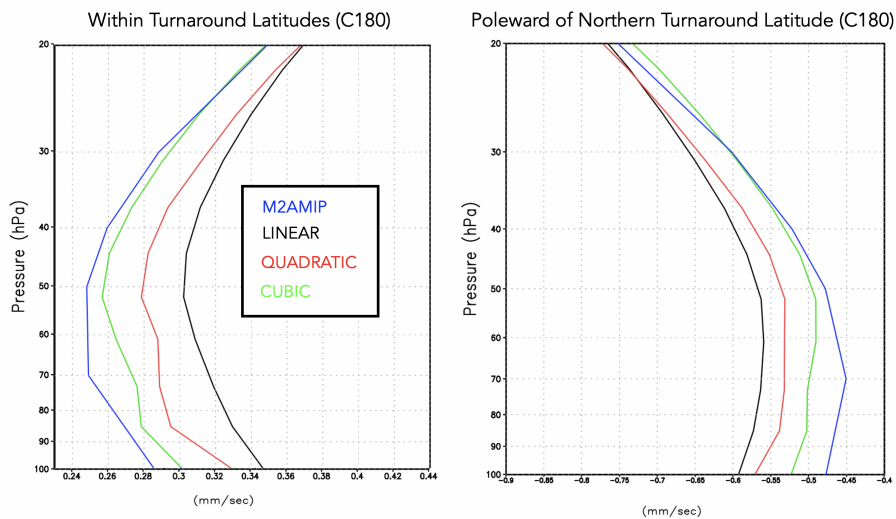


Figure C1. Left: The DJF climatological mean vertical residual mean velocity, w^* , averaged between the turnaround latitudes for the CTRL (cyan line; Table 2, row 1), LINEAR (green line; Table 2, row 5), and QUADRATIC (blue line; Table 2, row 6) experiments. M2AMIP is shown in black. Right: As in left panel, except averaged over latitudes poleward of the northern turnaround latitude. Results are shown for C180 experiments. **COLORS NEED CHANGING.**

C180 EMIP 30-yr DJF Climatology (Dec 1985 – Feb 2015)

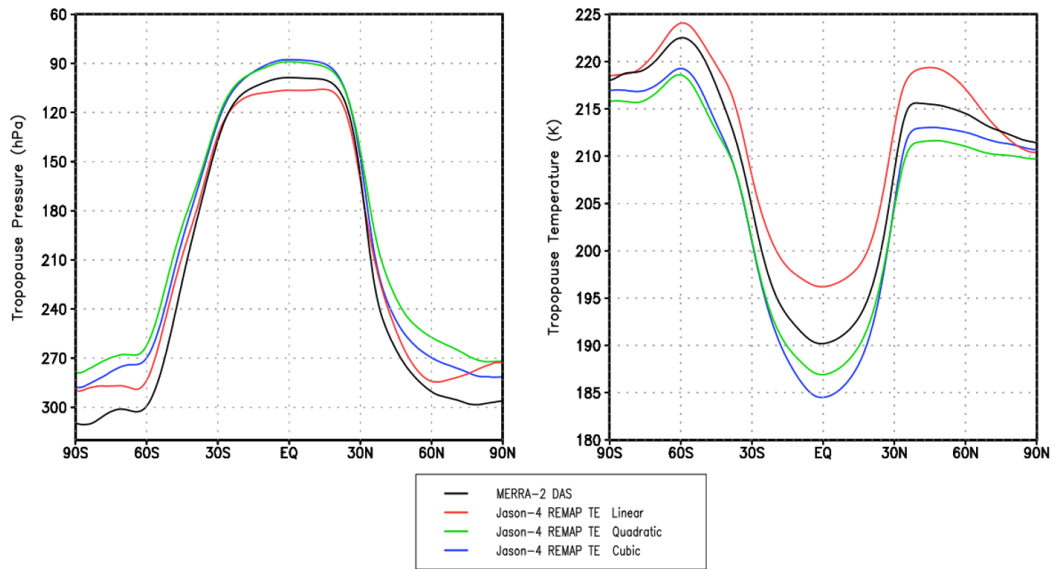


Figure D1. The DJF climatological mean tropopause pressure (left) and temperature (right) in the CUBIC (blue), QUADRATIC (green and LINEAR (red) experiments. MERRA-2 is shown in black. Results are presented for the C180 experiments.

634 Appendix D Tropopause Pressures

635 Appendix Figure D1 compares boreal winter tropopause pressures among the LIN-
636 EAR, QUADRATIC and CUBIC experiments, relative to MERRA-2.

637 Open Research Section

638 TBD

639 Acknowledgments

640 TBD

641 References

- 642 Abalos, M., Calvo, N., Benito-Barca, S., Garny, H., Hardiman, S. C., Lin, P., ...
643 others (2021). The brewer–dobson circulation in cmip6. *Atmospheric Chem-*
644 *istry and Physics*, *21*(17), 13571–13591.
- 645 Abalos, M., Orbe, C., Kinnison, D. E., Plummer, D., Oman, L. D., Jöckel, P., ...
646 others (2020). Future trends in stratosphere-to-troposphere transport in ccmi
647 models. *Atmospheric Chemistry and Physics*, *20*(11), 6883–6901.
- 648 Abalos, M., Randel, W. J., Kinnison, D. E., & Garcia, R. R. (2017). Using the arti-
649 ficial tracer e90 to examine present and future utls tracer transport in waccm.
650 *Journal of the Atmospheric Sciences*, *74*(10), 3383–3403.
- 651 Andrews, D., Holton, J., & Leovy, C. (1987). Middle Atmosphere Dynam-

- 652 ics. *Academic Press*, 60, 489. doi: 10.1175/1520-0469(2003)060<0103:
653 CEOOAL>2.0.CO;2
- 654 Arnold, N. P., Putman, W. M., & Freitas, S. R. (2020). Impact of resolution and
655 parameterized convection on the diurnal cycle of precipitation in a global
656 nonhydrostatic model. *Journal of the Meteorological Society of Japan. Ser. II.*
- 657 Boering, K. A., Wofsy, S., Daube, B., Schneider, H., Loewenstein, M., Podolske, J.,
658 & Conway, T. (1996). Stratospheric mean ages and transport rates from obser-
659 vations of carbon dioxide and nitrous oxide. *Science*, 274(5291), 1340–1343.
- 660 Butchart, N., Cionni, I., Eyring, V., Shepherd, T., Waugh, D., Akiyoshi, H., ...
661 others (2010). Chemistry–climate model simulations of twenty-first century
662 stratospheric climate and circulation changes. *Journal of Climate*, 23(20),
663 5349–5374.
- 664 Chiodo, G., & Polvani, L. M. (2019). The response of the ozone layer to quadru-
665 pled co₂ concentrations: Implications for climate. *Journal of climate*, 32(22),
666 7629–7642.
- 667 Chou, M.-D. (1990). Parameterizations for the absorption of solar radiation by o₂
668 and co₂ with application to climate studies. *Journal of Climate*, 3(2), 209–
669 217.
- 670 Chou, M.-D. (1992). A solar radiation model for use in climate studies. *Journal of*
671 *Atmospheric Sciences*, 49(9), 762–772.
- 672 Chou, M.-D., & Suarez, M. J. (1994). An efficient thermal infrared radiation param-
673 eterization for use in general circulation models.
- 674 Collow, A. B. M., Mahanama, S. P., Bosilovich, M. G., Koster, R. D., & Schubert,
675 S. D. (2017). *An evaluation of teleconnections over the united states in an*
676 *ensemble of amip simulations with the merra-2 configuration of the geos atmo-*
677 *spheric model* (Tech. Rep.).
- 678 Davis, N. A., Callaghan, P., Simpson, I. R., & Tilmes, S. (2022). Specified dynamics
679 scheme impacts on wave-mean flow dynamics, convection, and tracer transport
680 in cesm2 (waccm6). *Atmospheric Chemistry and Physics*, 22(1), 197–214.
- 681 Dietmüller, S., Eichinger, R., Garny, H., Birner, T., Boenisch, H., Pitari, G., ... oth-
682 ers (2018). Quantifying the effect of mixing on the mean age of air in ccmval-2
683 and ccmi-1 models. *Atmospheric Chemistry and Physics*, 18(9), 6699–6720.
- 684 Eichinger, R., Garny, H., Šácha, P., Danker, J., Dietmüller, S., & Oberländer-Hayn,
685 S. (2020). Effects of missing gravity waves on stratospheric dynamics; part 1:
686 climatology. *Climate Dynamics*, 54(5), 3165–3183.
- 687 Eluszkiewicz, J., Hemler, R. S., Mahlman, J. D., Bruhwiler, L., & Takacs, L. L.
688 (2000). Sensitivity of age-of-air calculations to the choice of advection scheme.
689 *Journal of the atmospheric sciences*, 57(19), 3185–3201.
- 690 Eyring, V., Lamarque, J.-F., Hess, P., Arfeuille, F., Bowman, K., Chipperfield,
691 M. P., ... others (2013). Overview of igac/sparc chemistry-climate model
692 initiative (ccmi) community simulations in support of upcoming ozone and
693 climate assessments. *SPARC newsletter*, 40(Januar), 48–66.
- 694 Freitas, S. R., Grell, G. A., Molod, A., Thompson, M. A., Putman, W. M., Santos e
695 Silva, C. M., & Souza, E. P. (2018). Assessing the grell-freitas convection
696 parameterization in the nasa geos modeling system. *Journal of Advances in*
697 *Modeling Earth Systems*, 10(6), 1266–1289.
- 698 Freitas, S. R., Putman, W. M., Arnold, N. P., Adams, D. K., & Grell, G. A. (2020).
699 Cascading toward a kilometer-scale gcm: Impacts of a scale-aware convection
700 parameterization in the goddard earth observing system gcm. *Geophysical*
701 *Research Letters*, 47(17), e2020GL087682.
- 702 Gelaro, R., McCarty, W., Suárez, M. J., Todling, R., Molod, A., Takacs, L., ...
703 others (2017). The modern-era retrospective analysis for research and applica-
704 tions, version 2 (merra-2). *Journal of climate*, 30(14), 5419–5454.
- 705 Gerber, E. P., & Manzini, E. (2016). The dynamics and variability model intercom-
706 parison project (dynvarmip) for cmip6: assessing the stratosphere–troposphere

- 707 system. *Geoscientific Model Development*, 9(9), 3413–3425.
- 708 Grell, G. A., & Freitas, S. R. (2014). A scale and aerosol aware stochastic convective
709 parameterization for weather and air quality modeling. *Atmospheric Chemistry
710 and Physics*, 14(10), 5233–5250.
- 711 Grooß, J.-U., & Russell III, J. M. (2005). A stratospheric climatology for o₃, h₂
712 o, ch₄, no_x, hcl and hf derived from haloe measurements. *Atmospheric chem-
713 istry and physics*, 5(10), 2797–2807.
- 714 Gupta, A., Gerber, E. P., & Lauritzen, P. H. (2020). Numerical impacts on tracer
715 transport: A proposed intercomparison test of atmospheric general circula-
716 tion models. *Quarterly Journal of the Royal Meteorological Society*, 146(733),
717 3937–3964.
- 718 Hall, T. M., & Plumb, R. A. (1994). Age as a diagnostic of stratospheric transport.
719 *Journal of Geophysical Research: Atmospheres*, 99(D1), 1059–1070.
- 720 Hall, T. M., Waugh, D. W., Boering, K. A., & Plumb, R. A. (1999). Evaluation
721 of transport in stratospheric models. *Journal of Geophysical Research: Atmo-
722 spheres*, 104(D15), 18815–18839.
- 723 Hardiman, S. C., Andrews, D. G., White, A. A., Butchart, N., & Edmond, I. (2010).
724 Using different formulations of the transformed eulerian mean equations and
725 eliasen–palm diagnostics in general circulation models. *Journal of the atmo-
726 spheric sciences*, 67(6), 1983–1995.
- 727 Hardiman, S. C., Butchart, N., & Calvo, N. (2014). The morphology of the brewer-
728 dobson circulation and its response to climate change in cmip5 simulations.
729 *Quarterly Journal of the Royal Meteorological Society*, 140(683), 1958–1965.
- 730 Haynes, P., McIntyre, M., Shepherd, T., Marks, C., & Shine, K. P. (1991). On the
731 “downward control” of extratropical diabatic circulations by eddy-induced
732 mean zonal forces. *Journal of the Atmospheric Sciences*, 48(4), 651–678.
- 733 Hegglin, M. I., Brunner, D., Peter, T., Hoor, P., Fischer, H., Staehelin, J., . . . Weers,
734 U. (2006). Measurements of no, no_y, n₂o, and o₃ during spurt: implica-
735 tions for transport and chemistry in the lowermost stratosphere. *Atmospheric
736 chemistry and physics*, 6(5), 1331–1350.
- 737 Holton, J. R., Haynes, P. H., McIntyre, M. E., Douglass, A. R., Rood, R. B., & Pfis-
738 ter, L. (1995). Stratosphere-troposphere exchange. *Reviews of geophysics*,
739 33(4), 403–439.
- 740 Holzer, M., & Hall, T. M. (2000). Transit-time and tracer-age distributions in geo-
741 physical flows. *Journal of the atmospheric sciences*, 57(21), 3539–3558.
- 742 Iacono, M. J., Delamere, J. S., Mlawer, E. J., Shephard, M. W., Clough, S. A., &
743 Collins, W. D. (2008). Radiative forcing by long-lived greenhouse gases:
744 Calculations with the aer radiative transfer models. *Journal of Geophysical
745 Research: Atmospheres*, 113(D13).
- 746 Ivy, D. J., Solomon, S., Calvo, N., & Thompson, D. W. (2017). Observed connec-
747 tions of arctic stratospheric ozone extremes to northern hemisphere surface
748 climate. *Environmental Research Letters*, 12(2), 024004.
- 749 Kouatchou, J., Molod, A., Nielsen, J., Auer, B., Putman, W., & Clune, T. (2015).
750 *Geos-5 chemistry transport model user’s guide* (Tech. Rep.).
- 751 Legras, B., Pisso, I., Berthet, G., & Lefèvre, F. (2004). Variability of the lagrangian
752 turbulent diffusivity in the lower stratosphere. *Atmospheric Chemistry and
753 Physics Discussions*, 4(6), 8285–8325.
- 754 Lin, S.-J. (2004). A “vertically lagrangian” finite-volume dynamical core for global
755 models. *Monthly Weather Review*, 132(10), 2293–2307.
- 756 Molod, A., Takacs, L., Suarez, M., & Bacmeister, J. (2015). Development of the
757 geos-5 atmospheric general circulation model: Evolution from merra to merra2.
758 *Geoscientific Model Development*, 8(5), 1339–1356.
- 759 Monge-Sanz, B., Chipperfield, M., Simmons, A., & Uppala, S. (2007). Mean age of
760 air and transport in a ctm: Comparison of different ecmwf analyses. *Geophys-
761 ical Research Letters*, 34(4).

- 762 Monge-Sanz, B. M., Bozzo, A., Byrne, N., Chipperfield, M. P., Diamantakis, M.,
 763 Flemming, J., . . . others (2022). A stratospheric prognostic ozone for seam-
 764 less earth system models: performance, impacts and future. *Atmospheric*
 765 *Chemistry and Physics*, *22*(7), 4277–4302.
- 766 Morgenstern, O., & Carver, G. D. (2001). Comparison of cross-tropopause transport
 767 and ozone in the upper troposphere and lower stratosphere region. *Journal of*
 768 *Geophysical Research: Atmospheres*, *106*(D10), 10205–10221.
- 769 Neu, J., Strahan, S., Braesicke, P., Douglass, A., Huck, P., Oman, L., . . . Tegtmeier,
 770 S. (2010). Sparc ccmval (2010), sparc report on the evaluation of chemistry-
 771 climate models: Chapter 5: Transport. SPARC.
- 772 Neu, J. L., & Plumb, R. A. (1999). Age of air in a “leaky pipe” model of strato-
 773 spheric transport. *Journal of Geophysical Research: Atmospheres*, *104*(D16),
 774 19243–19255.
- 775 Oehrlein, J., Chiodo, G., & Polvani, L. M. (2020). The effect of interactive ozone
 776 chemistry on weak and strong stratospheric polar vortex events. *Atmospheric*
 777 *Chemistry and Physics*, *20*(17), 10531–10544.
- 778 Orbe, C., Oman, L. D., Strahan, S. E., Waugh, D. W., Pawson, S., Takacs, L. L., &
 779 Molod, A. M. (2017). Large-scale atmospheric transport in geos replay simula-
 780 tions. *Journal of Advances in Modeling Earth Systems*, *9*(7), 2545–2560.
- 781 Orbe, C., Rind, D., Jonas, J., Nazarenko, L., Faluvegi, G., Murray, L. T., . . . oth-
 782 ers (2020). Giss model e2. 2: A climate model optimized for the middle
 783 atmosphere—2. validation of large-scale transport and evaluation of cli-
 784 mate response. *Journal of Geophysical Research: Atmospheres*, *125*(24),
 785 e2020JD033151.
- 786 Orbe, C., Yang, H., Waugh, D. W., Zeng, G., Morgenstern, O., Kinnison, D. E., . . .
 787 others (2018). Large-scale tropospheric transport in the chemistry–climate
 788 model initiative (ccmi) simulations. *Atmospheric Chemistry and Physics*,
 789 *18*(10), 7217–7235.
- 790 Pan, L. L., Wei, J., Kinnison, D., Garcia, R., Wuebbles, D., & Brasseur, G. P.
 791 (2007). A set of diagnostics for evaluating chemistry-climate models in the ex-
 792 tratropical tropopause region. *Journal of Geophysical Research: Atmospheres*,
 793 *112*(D9).
- 794 Pawson, S., Stajner, I., Kawa, S. R., Hayashi, H., Tan, W.-W., Nielsen, J. E., . . .
 795 Livesey, N. J. (2007). Stratospheric transport using 6-h-averaged winds from
 796 a data assimilation system. *Journal of Geophysical Research: Atmospheres*,
 797 *112*(D23).
- 798 Plumb, R. A. (1985). On the three-dimensional propagation of stationary waves.
 799 *Journal of Atmospheric Sciences*, *42*(3), 217–229.
- 800 Plumb, R. A. (1996). A “tropical pipe” model of stratospheric transport. *Journal of*
 801 *Geophysical Research: Atmospheres*, *101*(D2), 3957–3972.
- 802 Plumb, R. A. (2002). Stratospheric transport. *Journal of the Meteorological Society*
 803 *of Japan. Ser. II*, *80*(4B), 793–809.
- 804 Polvani, L. M., Waugh, D. W., Correa, G. J., & Son, S.-W. (2011). Stratospheric
 805 ozone depletion: The main driver of twentieth-century atmospheric circulation
 806 changes in the southern hemisphere. *Journal of Climate*, *24*(3), 795–812.
- 807 Prather, M. J., Zhu, X., Tang, Q., Hsu, J., & Neu, J. L. (2011). An atmospheric
 808 chemist in search of the tropopause. *Journal of Geophysical Research: Atmo-*
 809 *spheres*, *116*(D4).
- 810 Rood, R. B. (1987). Numerical advection algorithms and their role in atmospheric
 811 transport and chemistry models. *Reviews of geophysics*, *25*(1), 71–100.
- 812 Rosenlof, K. H. (1995). Seasonal cycle of the residual mean meridional circulation
 813 in the stratosphere. *Journal of Geophysical Research: Atmospheres*, *100*(D3),
 814 5173–5191.
- 815 Son, S.-W., Tandon, N. F., Polvani, L. M., & Waugh, D. W. (2009). Ozone hole and
 816 southern hemisphere climate change. *Geophysical Research Letters*, *36*(15).

- 817 Strahan, S., Douglass, A., & Newman, P. (2013). The contributions of chemistry
818 and transport to low arctic ozone in march 2011 derived from aura mls obser-
819 vations. *Journal of Geophysical Research: Atmospheres*, *118*(3), 1563–1576.
- 820 Thiele, G., & Sarmiento, J. (1990). Tracer dating and ocean ventilation. *Journal of*
821 *Geophysical Research: Oceans*, *95*(C6), 9377–9391.
- 822 Waugh, D., & Hall, T. (2002). Age of stratospheric air: Theory, observations, and
823 models. *Reviews of Geophysics*, *40*(4), 1–1.